

Investigating high-energy Hermite-Gauss and vortex laser generation in Alexandrite

Enlin Cai^{1,2,3}, Shuaiyi Zhang⁴, Tao Li⁵, Jie Wang², and Min Chen^{1,2,3}

¹ *Shanghai Institute of Applied Physics, Chinese Academy of Sciences, Shanghai, China*

² *Shanghai Advanced Research Institute, Chinese Academy of Sciences, Shanghai, China*

³ *University of Chinese Academy of Sciences, Beijing, China*

⁴ *Shandong Advanced Optoelectronic Materials and Technologies Engineering Laboratory, School of Mathematics and Physics, Qingdao University of Science & Technology, Qingdao, China*

⁵ *School of Information Science and Engineering, and Shandong Provincial Key Laboratory of Laser Technology and Application, Shandong University, Qingdao, China*

Abstract

This paper presents an investigation of the secondary saturation characteristics of a HfTe₂ saturable absorber. Pulse energies of 5.85 mJ and 7.4 mJ were demonstrated with a high-order Hermite-Gaussian (HG) laser and a vortex laser, respectively, using Alexandrite as the gain medium. To the best of our knowledge, these are the highest pulse energies directly generated with HG and vortex lasers. To broaden the applications of high-energy pulsed HG and vortex lasers, wavelength tuning over a range of 40 nm was achieved using an etalon.

Key words: Structured light field; High-energy pulse laser; Reverse saturable absorption;

Wavelength tuning

This peer-reviewed article has been accepted for publication but not yet copyedited or typeset, and so may be subject to change during the production process. The article is considered published and may be cited using its DOI.

This is an Open Access article, distributed under the terms of the Creative Commons Attribution licence (<https://creativecommons.org/licenses/by/4.0/>), which permits unrestricted re-use, distribution, and reproduction in any medium, provided the original work is properly cited.

10.1017/hpl.2025.34

Correspondence to: Min Chen, Shanghai Advanced Research Institute, Chinese Academy of Sciences, Shanghai 201800, China. Email: chenm@sari.ac.cn. Shuaiyi Zhang, Shandong Advanced Optoelectronic Materials and Technologies Engineering Laboratory, School of Mathematics and Physics, Qingdao University of Science & Technology, Qingdao 266061, China. Email: shuaiyi163@163.com;

1. Introduction

The intensity and phase distributions of high-order Hermite-Gaussian (HG) beams allow them to transmit more information than Gaussian beams, and so they have important applications in field such as laser capacity communications, optical measurement, and optical manipulation [1-4]. In addition, high-order HG beams can be transformed into vortex beams carrying an orbital angular momentum of lh (with l the quantum number and \hbar the reduced Planck constant), further broadening their applicability [5-7]. Structured light field generated by high-energy high-order HG lasers have a great deal of benefits over unstructured light [8-12]. However, high-order HG lasers have thus far primarily been confined to a low energy range, owing to the limitations imposed by the damage threshold, and the efficiency of existing generation techniques. The extra-cavity generation method for structured light field relies on phase modulation, which has proven to be inadequate for producing a stably propagating high-order HG mode laser. This limitation stems from the fact that such extra-cavity implementations merely execute the user-programmed photonic design without demonstrating intrinsic evolutionary capabilities, thereby failing to achieve the dynamic characteristics necessary of an active system. Additionally, the converters employed for this method are not sufficiently robust to withstand the impact of a high-energy laser [13,14]. The intra-cavity method primarily achieves vortex laser generation by adjusting the gain of different modes. However, etching spot-defects on the input mirror has not yet succeeded in producing high-order HG lasers, and this technique typically reduces the utilization efficiency of the pump laser [15-19]. Consequently, it is essential to develop a method that can generate high-order

HG lasers with stable propagation and high efficiency, while remaining unaffected by damage threshold limitations. In 2024, Tao et al. [20] theoretically demonstrated that high-order HG lasers with low loss characteristics can be generated using a segmented mirror. This indicates that etching stripes of various shapes and dimensions onto the output mirror is a feasible method for the generation of high-order HG lasers, without affecting the incidence efficiency of the pump laser.

Suitable gain media and laser regulation methods are indispensable for the production of high-energy pulsed lasers. Within the visible spectrum, Alexandrite ($\text{Cr}^{3+}:\text{BeAl}_2\text{O}_4$) is regarded as an exceptional medium for creating a high-energy pulsed laser, as a result of its superior thermal conductivity, high saturation energy density, robust damage threshold, and long fluorescence lifetime [21-23]. Furthermore, the effective gain cross-section of Alexandrite crystals increases with temperature, facilitating efficient high-power pumping. In 2023, Liang et al. [24] successfully obtained a high-energy pulse of 2.6 mJ in Alexandrite using acousto-optic Q-switching, highlighting the potential of this method for high-energy operation. Passive Q-switching (PQS) is an effective technique for producing pulsed lasers, offering the advantages of a compact design which does not need an external driver. However, PQS typically struggles to achieve high pulse energies, owing to the low saturable fluence of saturable absorbers (SAs), particularly when using two-dimensional (2D) SAs [25-27]. It is worth noting that light absorption by excited state energy levels causes the transmittance of specific 2D materials to decrease only under excitation by extremely high-intensity light. This phenomenon is known as reverse saturable absorption [28]. Nevertheless, excited state absorption in 2D materials can also reach saturation, in a condition referred to as secondary saturation. Compared with ground state absorption saturation, a significantly higher excitation intensity is required to achieve this condition in an excited state. Therefore, SAs with secondary saturation characteristics typically exhibit a higher saturable

fluence, which may alleviate the challenges of generating high-energy pulsed lasers through the PQS method.

In this paper, the secondary saturation characteristics of a high quality, custom-made HfTe_2 SA, which has a high damage threshold, were demonstrated using the open aperture Z-scan method. By employing a defected output mirror and a reverse saturable absorber (RSA) HfTe_2 , high-order HG pulsed lasers of various orders with a maximal single pulse energy of 5.85 mJ, and a vortex laser with a single pulse energy of 7.4 mJ, were obtained in Alexandrite. The repetition rates of these lasers were 262 Hz and 196 Hz, respectively. To expand the applications of high-energy structured lasers, wavelength tuning within the range 747-787 nm was successfully accomplished using an etalon.

2. Experimental setup

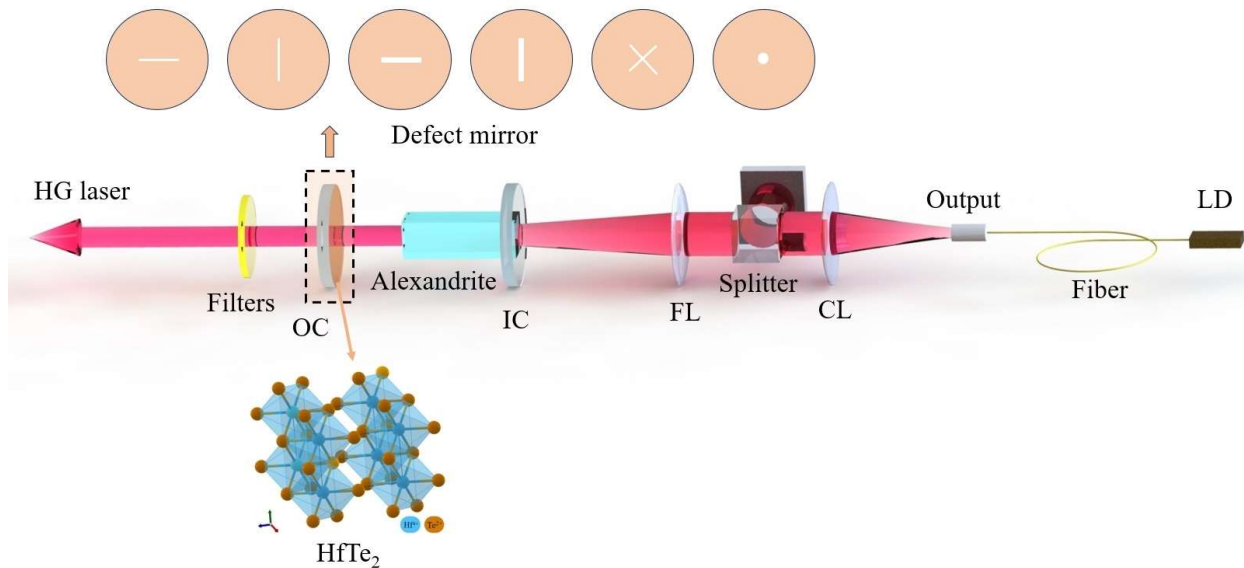


Figure 1. Schematic diagram of the generation of high-energy Hermite-Gauss laser. LD: laser diode; CL: collimating lens; FL: focusing lens; IC: input coupling; OC: output coupling. Inset: defected stripes at OC and crystal structure of HfTe_2 .

A schematic diagram of the high-energy HG Alexandrite laser is shown in Fig. 1. The pump laser is a laser diode (LD) with an emission wavelength of 638 nm, offering higher quantum efficiency compared to other pump wavelengths. Owing to the polarization-dependent absorption properties of Alexandrite, the pump laser is directed through a polarization beam splitter to enhance the pumping efficiency. The coupling system consists of a collimating lens (CL) and a focusing lens (FL), with focal lengths of 100 mm and 50 mm, respectively. The pump laser is focused through a coupling system, generating a circular spot with a diameter of 200 μm within the crystal. Both the input coupling (IC) and the output coupling (OC) are implemented using plane mirrors to maintain the beam quality of the output laser. The Alexandrite crystal, with a Cr^{3+} doping concentration of 0.2%, was precision-cut to dimensions of $3 \times 3 \times 8 \text{ mm}^3$ and finely polished. The optical path surfaces are coated with a high transmittance for a 755 nm laser. The transmittance of the OC is fixed at 3% and defect stripes of diverse widths and shapes were introduced, as shown in Fig. 1, in order to permit the laser to pass through without being reflected, such that only the laser modes that overlap with the non-defected area can be effectively amplified. The output laser is directed through a bandpass filter to obtain high-purity HG modes, free from interference with the pump laser. The HfTe_2 absorber was coated onto the OC to achieve Q-switching and to minimize resonant cavity loss.

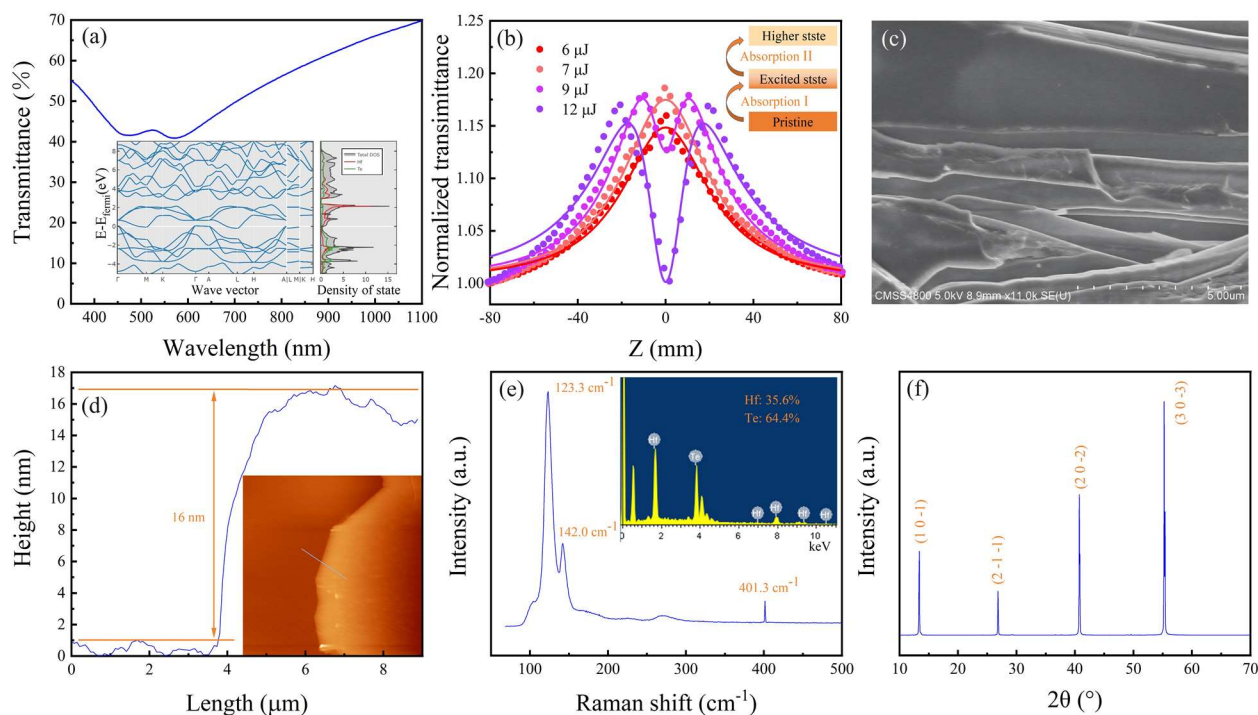


Figure 2. (a) Light transmittance of HfTe₂ in the wavelength range of 350-1100 nm; Inset: energy band structure and density of states of HfTe₂; (b) Saturation absorption and reverse saturation absorption results of HfTe₂ based on open aperture Z-scan; Inset: the principle of saturation absorption and reverse saturation absorption process; (c) Surface microstructure of HfTe₂ by SEM; (d) Thickness of single-layer HfTe₂ nanosheets by AFM; Inset: the AFM height image in the area of 30 × 30 μm². (e) Raman spectrum of HfTe₂; Inset: the EDS element analysis; (f) XRD patterns of HfTe₂.

The optical transmittance of HfTe₂ across the wavelength range 350-1100 nm is shown in Fig. 2(a), demonstrating its strong absorption of visible and near-infrared light. The band energy structure and electron density of HfTe₂ are depicted in the inset of Fig. 2(a), revealing its zero-bandgap structure. Upon incidence of a laser on HfTe₂, electrons in the pristine state are excited to the excited state (Absorption I). Increasing the incident laser power causes a greater number of electrons to populate the excited state. Due to Pauli blocking, which limits the electron occupation in this state, Absorption I reaches saturation and the material ceases to absorb additional laser energy. However, under excitation from a stronger laser, electrons in the excited state will

transition to a higher energy state (Absorption II). This process is known as reverse saturation absorption. With further increases in incident laser intensity, the higher energy state may also become saturated as a result of electron accumulation and the wide energy band gap, which impedes the relaxation process from the higher state back to the excited state, thereby ceasing further laser absorption. The characteristics of saturable absorption and reverse saturation absorption under high-energy excitation are demonstrated in Fig. 2(b) via the open aperture Z-scan method with an 800 nm femtosecond laser, confirming that HfTe₂ exhibits reverse saturation absorption properties. Figure 2(c) presents the surface microstructure of HfTe₂, as examined by scanning electron microscopy (SEM), clearly showing its layered structure. The height of a single-layer HfTe₂ nanosheet obtained by mechanical exfoliation, and measured by atomic force microscopy (AFM), was 16 nm, as shown in Fig. 2(d). The purity of HfTe₂ was analyzed by Raman spectroscopy and an Energy Dispersive Spectrometer (EDS), as shown in Fig. 2(e) and the inset. The peaks of the Raman spectrum are located at 123.3 cm⁻¹, 142.0 cm⁻¹, and 401.3 cm⁻¹, corresponding to the characteristic Raman peaks of HfTe₂. The EDS results indicate that the composition consists of 35.6% Hf and 64.4% Te, with no other elements detected. The growth direction of HfTe₂ was characterized by X-ray diffraction (XRD), with diffraction peaks observed at 2θ angles of 13.4°, 26.8°, 40.8°, and 55.4°, corresponding to the (1, 0, -1), (2, -1, -1), (2, 0, -2), and (3, 0, -3) growth directions, respectively, as shown in Fig. 2(f).

3. Characteristics of high-energy Structured light field

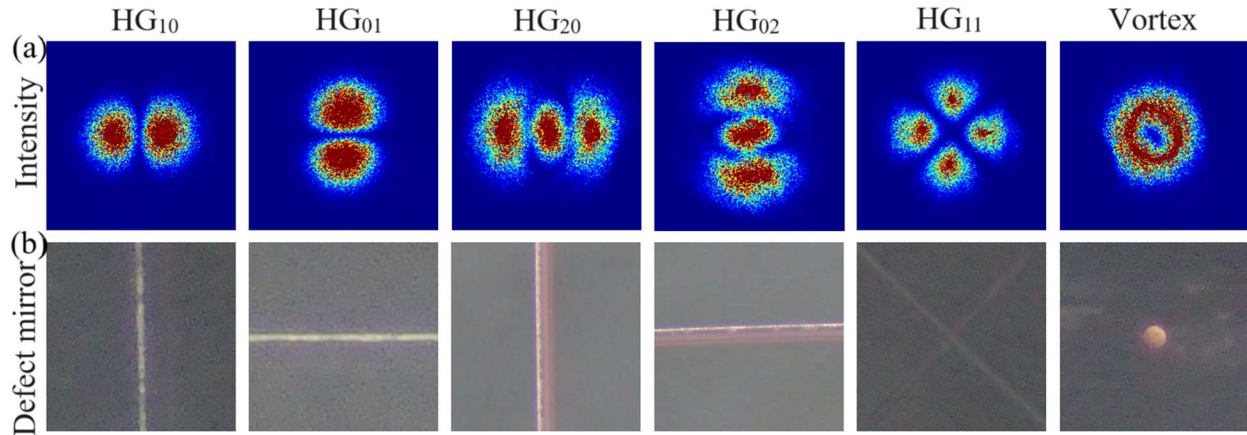


Figure 3. (a) The far-field intensity distribution of Hermite-Gauss laser of different orders and vortex laser; (b) The corresponding defected areas on the output coupling mirror.

The far-field intensity patterns of HG lasers of different orders and their corresponding defects on the OC are shown, respectively, in Fig. 3(a) and Fig. 3(b). The defects, introduced by mechanical etching, allow the laser to pass through without undergoing oscillation. The etched defects are placed on a red-light source and observed under a microscope. The red light can pass through the defects, appearing as bright areas, while the non-defect regions remain dark due to reflection from the film, as illustrated in Fig. 3(b). The intensity distribution of the HG laser is recorded by a CCD at a distance of 5 m in the far-field, with the corresponding laser divergence angle less than 5 mrad. With etched straight lines with a width of 20 μm in the vertical and horizontal directions, the laser is capable of generating HG₁₀ and HG₀₁ modes, respectively. As the defect width is increased to 60 μm , HG₂₀ and H₀₂ modes can be excited. Through the orthogonal cross-etching of two defect stripes, the laser is optimized to produce the HG₁₁ mode. In addition, by etching a circular hole in the OC, the laser can produce a ring-shaped vortex laser. However, due to spot size limitations, wider defects inhibit efficient laser oscillation, preventing the generation of higher order HG modes.

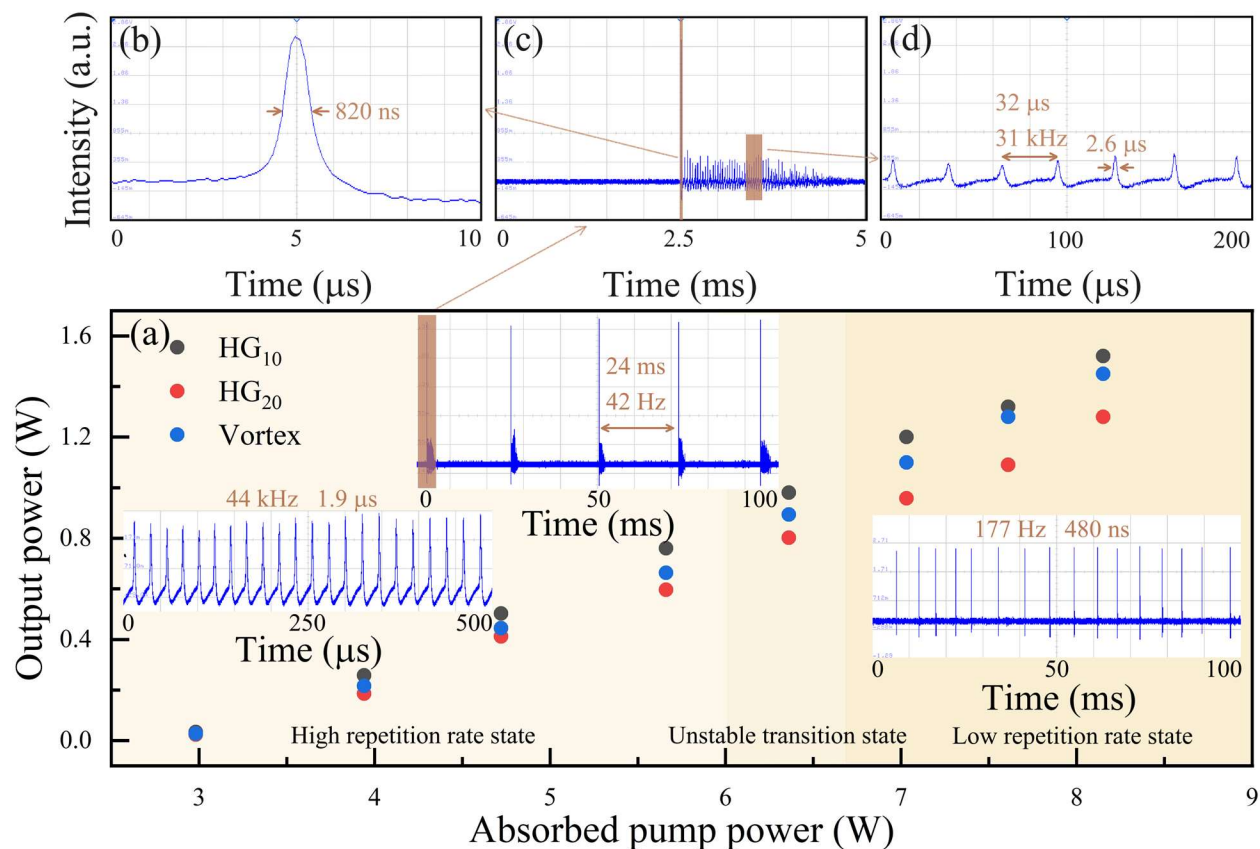


Figure 4. (a) Output characteristics of high-energy HG₁₀, HG₂₀ laser and vortex laser; Transition state pulse of HG₁₀ laser at (b) 10 μs; (c) 5 ms; (d) 200 μs scale.

The output pulse characteristics of the HG and vortex laser at different modes are shown in Fig. 4. Since the HG₁₀ and HG₀₁, HG₂₀ and HG₀₂, as well as HG₁₁ and vortex modes exhibit similar output power, repetition rate and pulse width, this work only presents the laser characteristics of the HG₁₀, HG₂₀, and vortex modes. The vortex laser operates in two stable states characterized by a high repetition rate state (>10 kHz) and a low repetition rate state (<300 Hz), as well as an unstable transition state, as described in Fig. 4(a). The threshold absorbed pump power is 3.0 W, and it operates in the high repetition rate state until the absorbed pump power exceeds 6.0 W. As the absorbed pump power increases, the repetition rate increases and the pulse width decreases gradually within the high repetition rate state. For the HG₁₀ mode, the maximum repetition rate reaches 44 kHz with a pulse width of 1.9 μs at 6.0 W of absorbed pump power, as shown in Fig.

4(a). As the absorbed pump power exceeds 6.0 W, Absorption I reaches a supersaturated state, resulting in high repetition rate pulses, and the laser enters an unstable transition state. During the transition state, while emitting high-energy, high repetition rate pulses, Absorption II also consumes the excited state electrons, causing Absorption I to no longer remain saturated. Consequently, the high repetition rate pulses reappear, as shown in Fig. 4(a). As the pump power increases, excited state is populated more rapidly, effectively sustaining a continuous saturation state, which results in the disappearance of the high repetition rate pulses. The low repetition rate pulse interval in the transition state is 24 ms, corresponding to a repetition rate of 42 Hz, with a pulse width of 820 ns, as depicted in Fig. 4(b). The high repetition rate pulses in this state have a repetition rate of 31 kHz and a pulse width of 2.6 μ s. Notably, the repetition rate of the high repetition rate pulses in the unstable transition state is lower than that in the high repetition rate state. This reduction is due to Absorption II decreasing the transmittance of the SA during the modulation of the high repetition rate pulse. The repetition rate of the low repetition rate pulse in the unstable transition state is also lower than that in the low repetition rate state, because the high repetition rate pulse consumes electrons in the excited state. When the absorbed pump power exceeds 6.2 W, Absorption I remains in a supersaturated state, and pulse generation depends exclusively on modulation by Absorption II, leading to low repetition rate pulses. Figure 4(a) illustrates a typical low repetition rate pulse with a repetition rate of 177 Hz and a pulse width of 480 ns, demonstrating superior stability in both pulse repetition and intensity compared to the high repetition rate pulses.

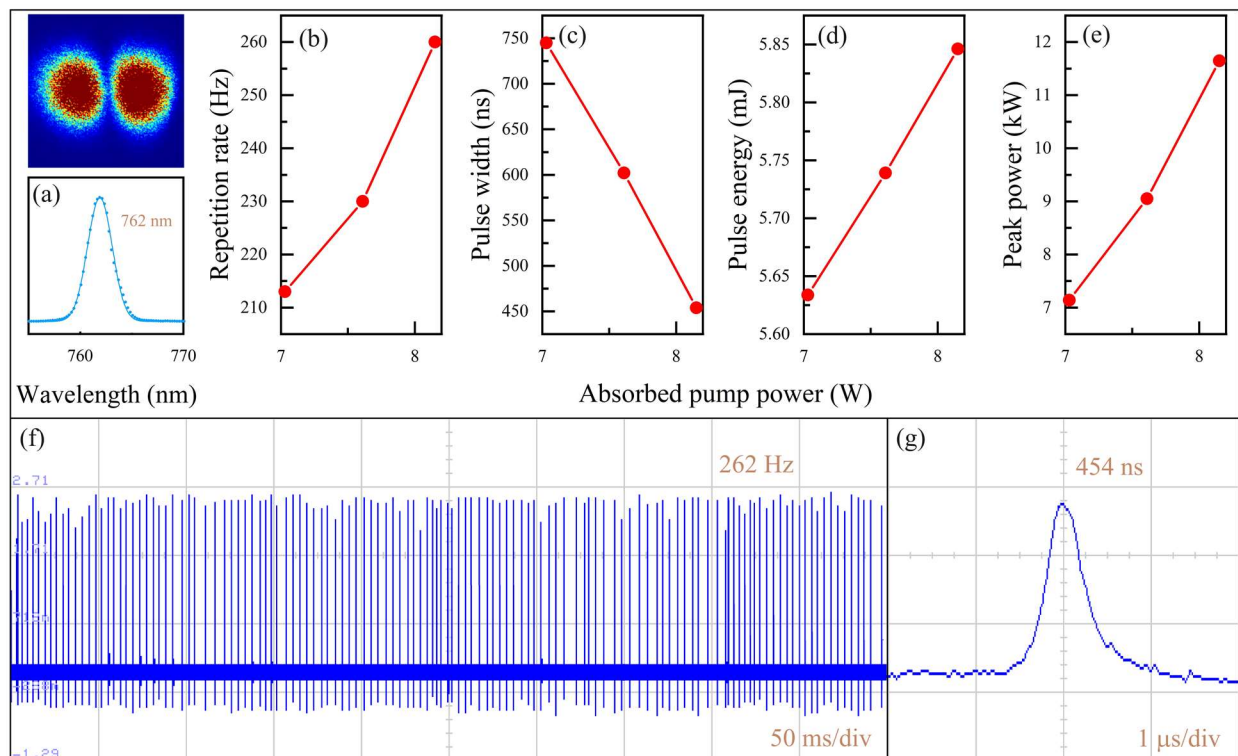


Figure 5. (a) Spectrum; (b) Repetition rate; (c) Pulse width; (d) Pulse energy; (e) Peak power of HG₁₀ mode versus absorbed pump power at low repetition rate state; (f) Typical Q-switched pulse train and (g) temporal pulse shape of HG₁₀ mode at maximum average output power.

The low repetition rate state pulse laser characteristics of the HG₁₀ mode are presented in Fig. 5. Figure 5(a) shows the spectrum of the Q-switched pulse laser, with a central wavelength at 762 nm and a full width at half maximum (FWHM) of 3 nm at the maximum absorbed pump power of 8.15 W. As the absorbed pump power increases, the repetition rate increases while the pulse width decreases gradually. When the absorbed pump power was 8.15 W, the maximum repetition rate and the narrowest pulse width were 262 Hz and 454 ns, respectively, as depicted in Figs. 5(f) and (g). The single pulse energy and peak power also increased gradually with the absorbed pump power, and the maximum pulse energy reached 5.85 mJ, corresponding to a peak power of 11.6 kW. The single pulse energy density and peak power density in the gain medium were 12.2 J/mm² and 24.3 MW/mm², respectively. Notably, the performance of the HfTe₂ SA is not compromised

by the impact of such a high-energy pulse. Typical pulse trains and temporal pulse profile are displayed in Figs. 5(f) and (g) in the time ranges of 0.5 s and 4 μ s. Figure 5(f) demonstrates that the pulse train has good repeatability and relatively consistent peak intensity. The remarkable pulse stability originates from two key aspects. Firstly, the high saturation intensity of the excited state absorption process increases the cavity loss, which promotes the generation of stable pulses and provides substantial fault tolerance. Secondly, the intrinsic stability of the material structure combined with its well-defined energy level structure, ensures consistent laser performance.

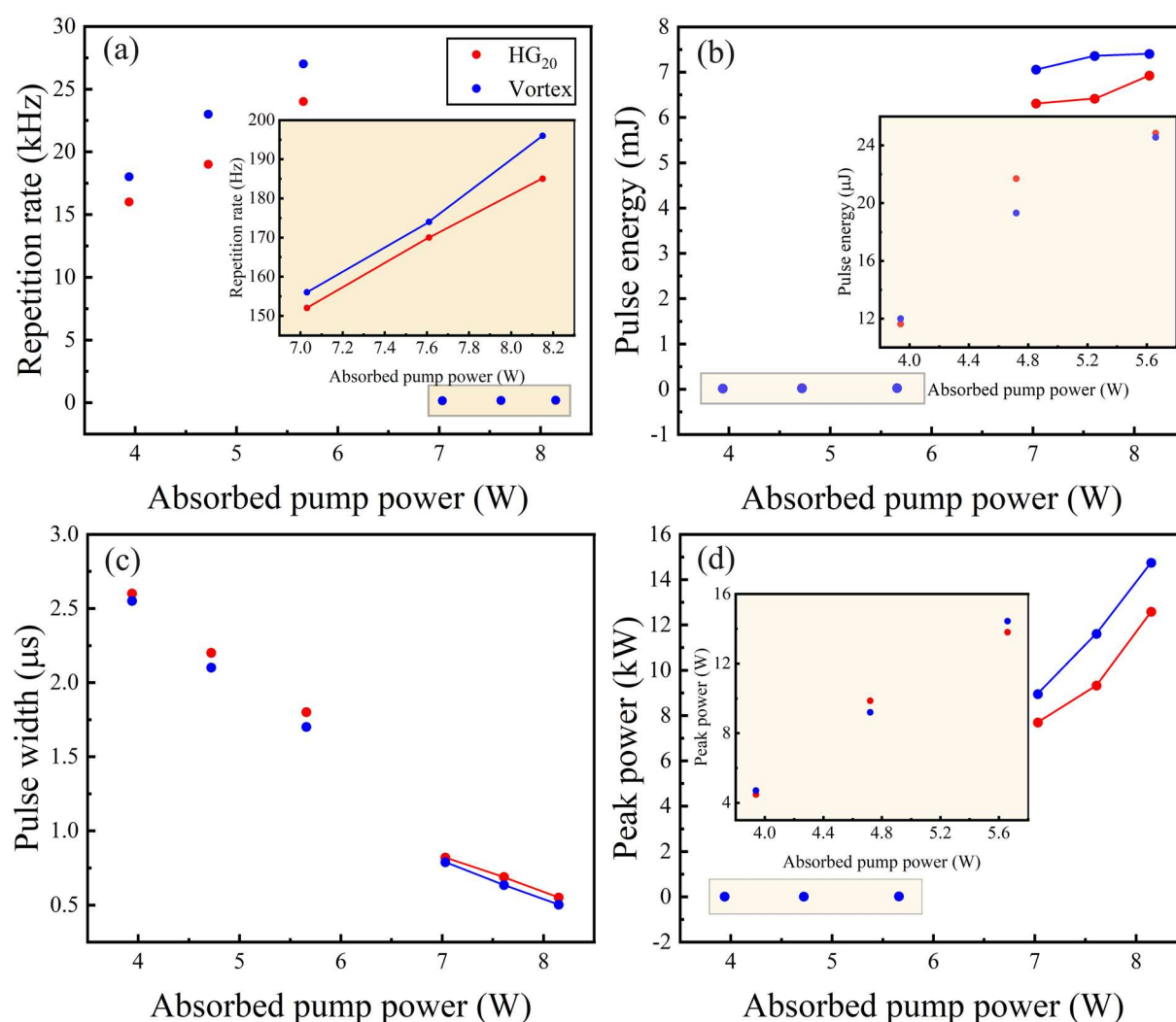


Figure 6. (a) Repetition rate; (b) Pulse energy; (c) Pulse width; (d) Peak power of HG₂₀ and vortex mode laser versus absorbed pump power.

The laser characteristics of the HG₂₀ and vortex modes are shown in Fig. 6. Figure 6(a) illustrates the variation of the repetition rate with absorbed pump power in both the high and low repetition rate states. In the high repetition rate state, the highest repetition rates were 24 kHz for the HG₂₀ mode and 28 kHz for the vortex mode, respectively, while these rates dropped sharply to 185 Hz and 196 Hz in the low repetition rate mode. The corresponding pulse energy also increased from 24.8 μ J to 6.92 mJ for the HG₂₀ mode and from 24.6 μ J to 7.40 mJ for the vortex mode, respectively, as depicted in Fig. 6(b), proving that Absorption II has a higher saturation flux and can accommodate more electrons due to its wider energy band. As shown in Fig. 6(c), the pulse width of both the HG₂₀ and vortex modes decreased slowly with increasing absorbed pump power, even across different states. The narrowest pulse widths reached 550 ns for the HG₂₀ mode and 502 ns for the vortex mode at the maximum absorbed pump power of 8.15 W.

Table 1. Comparative Characteristics of Q-switched high-order HG and Vortex mode laser

Mode	Wavelength	Gain medium (SA)	Output power	Pulse energy	Reference
HG	1064 nm	Nd:YAG (Cr:YAG)	1.32 W	22 μ J	[29]
HG	1079 nm	Nd:LYSO (Cr:YAG)	1.96 W	63 μ J	[30]
HG	1064 nm	Nd:YAG (Cr:YAG)	780 mW	3 μ J	[31]
HG	2018.3 nm	Tm:LuYAG (Active)	870 mW	1.51 mJ	[32]
Vortex	607 nm	Pr:YLF (Co:ASL)	139 mW	0.89 μ J	[33]
Vortex	639 nm	Pr:YLF (Co:ASL)	1.35 W	2.5 μ J	[34]
Vortex	1064 nm	Nd:YAG (Ag:LNOI)	130 mW	23.4 nJ	[35]
Vortex	1064 nm	Nd:YAG (Cr:YAG)	760 mW	18 μ J	[36]
Vortex	1063 nm	Nd:GdVO ₄ (Active)	9.38 W	469 μ J	[37]

Vortex	1647.7 nm	Er:LuYAG (Active)	940 mW	660 μ J	[38]
Vortex	1937.9 nm	Tm:YAP (Self)	83 mW	1.1 μ J	[39]
Vortex	2 μ m	Tm:YALO ₃ (Self)	4.8 W	38.8 μ J	[40]
HG	762 nm	Alexandrite (HfTe ₂)	1.52 W	5.85 mJ	This work
Vortex	762 nm	Alexandrite (HfTe ₂)	1.48 W	7.40 mJ	This work

Table 1 summarizes the characteristics of typical Q-switched high-order HG and vortex lasers. It can be seen that our experimental approach yields the highest pulse energy compared with other gain media and modulation methods. Nonetheless, it is particularly appropriate for the generation of high-energy HG pulses at short wavelength.

4. Wavelength tuning characteristics

Since a 750-785 nm laser corresponds to the absorption peak of Rb atoms, and has a deeper penetration depth in biological tissues, this wavelength range has a wide range of applications including laser medical treatment, cold atoms, and laser pumping^[41-50]. In particular, the 780 nm vortex laser has indispensable applications such as cold atomic clocks, hot atomic steam, and cold atom storage, but it can only be produced through extra-cavity modulation^[42,43]. To expand the utility of high-energy HG and vortex lasers, an etalon was employed for wavelength tuning based on an Alexandrite crystal, which has a wide emission spectrum, as shown in Fig. 7(b).

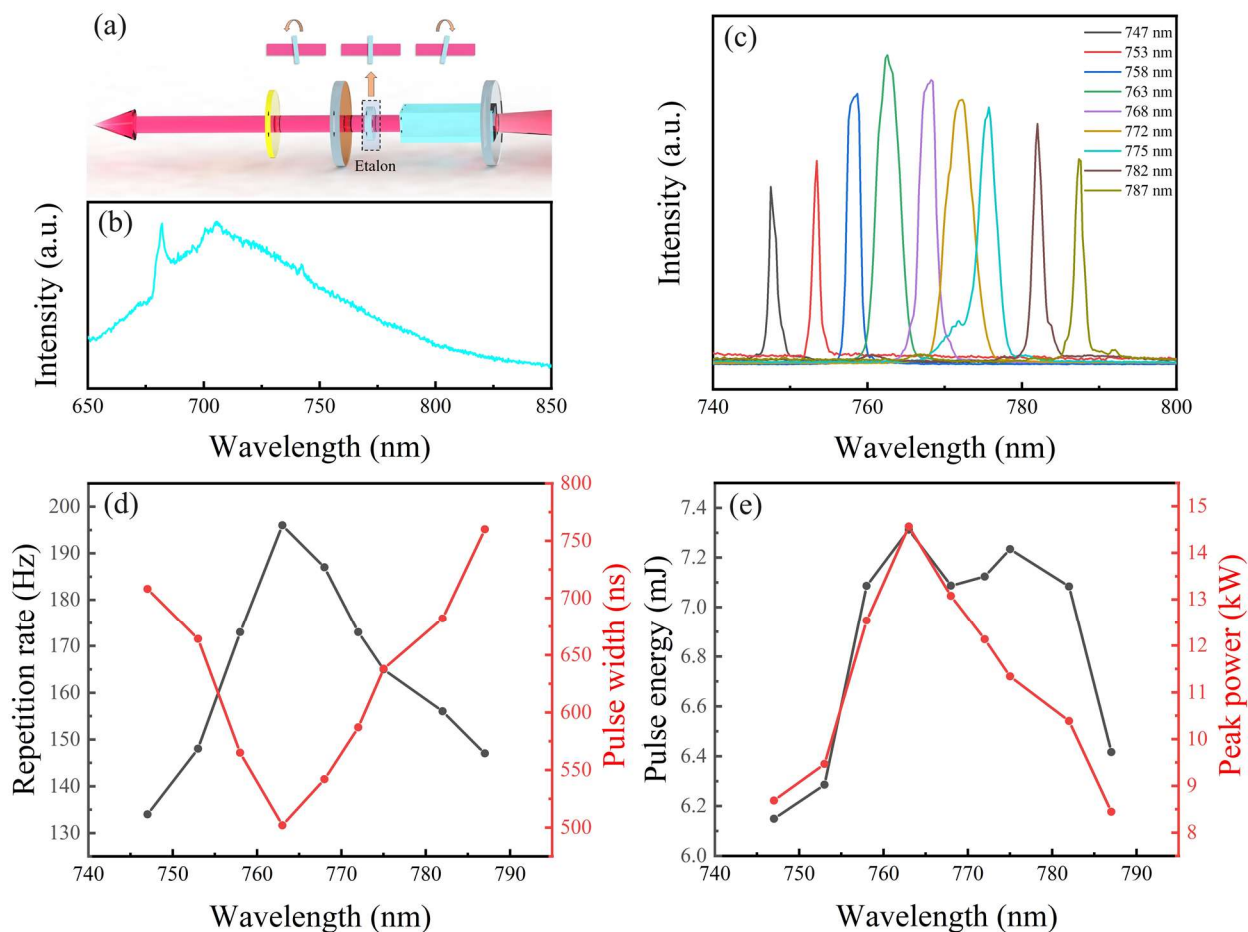


Figure 7. (a) Schematic diagram of wavelength tunable Q-switched vortex laser based on etalon; (b) Fluorescence spectrum of Alexandrite excited by 638 nm pump laser; (c) Laser spectra and relative intensities at different wavelengths within the Alexandrite wavelength tuning range; (d) Repetition rate and Pulse width; (e) Pulse energy and Peak power of passive Q-switching vortex laser versus wavelength.

The schematic diagram of a wavelength-tunable Q-switched vortex Alexandrite laser is depicted in Fig. 7(a). By utilizing a 0.2 mm thick etalon rotated within a tilt angle of 10° , continuous wavelength tuning can be achieved across the range of 747-787 nm. The relative intensity and full width at half maximum (FWHM) at different wavelengths are shown in Fig. 7(c). The FWHM of the spectrum is 3 nm at a central wavelength of 763 nm, while it narrows to 1 nm at the wavelengths of 747 nm and 787 nm due to the optical filtering effect of the etalon. Additionally, Figure 7 (d) presents the corresponding repetition rates and pulse widths at various

wavelengths at an absorbed pump power of 8.15 W. As the intra-cavity power diminishes, the repetition rate decreases and the pulse width increases. The repetition rate and pulse width of the 747 nm pulsed vortex laser were 134 Hz and 708 ns, respectively, while those of the 787 nm pulsed vortex laser were 147 Hz and 760 ns, respectively. The pulse energy and peak power show a dependence on the gain during the process of wavelength tuning. As shown in Fig. 7(e), the pulse energy and peak power of the 747 nm pulsed vortex laser were 6.15 mJ and 8.69 kW, respectively. Meanwhile, for the 787 nm pulsed vortex laser, the pulse energy and peak power were 6.42 mJ and 8.44 kW, respectively. The wavelength tuning range was restricted by the coating constraints of the resonant cavity mirrors.

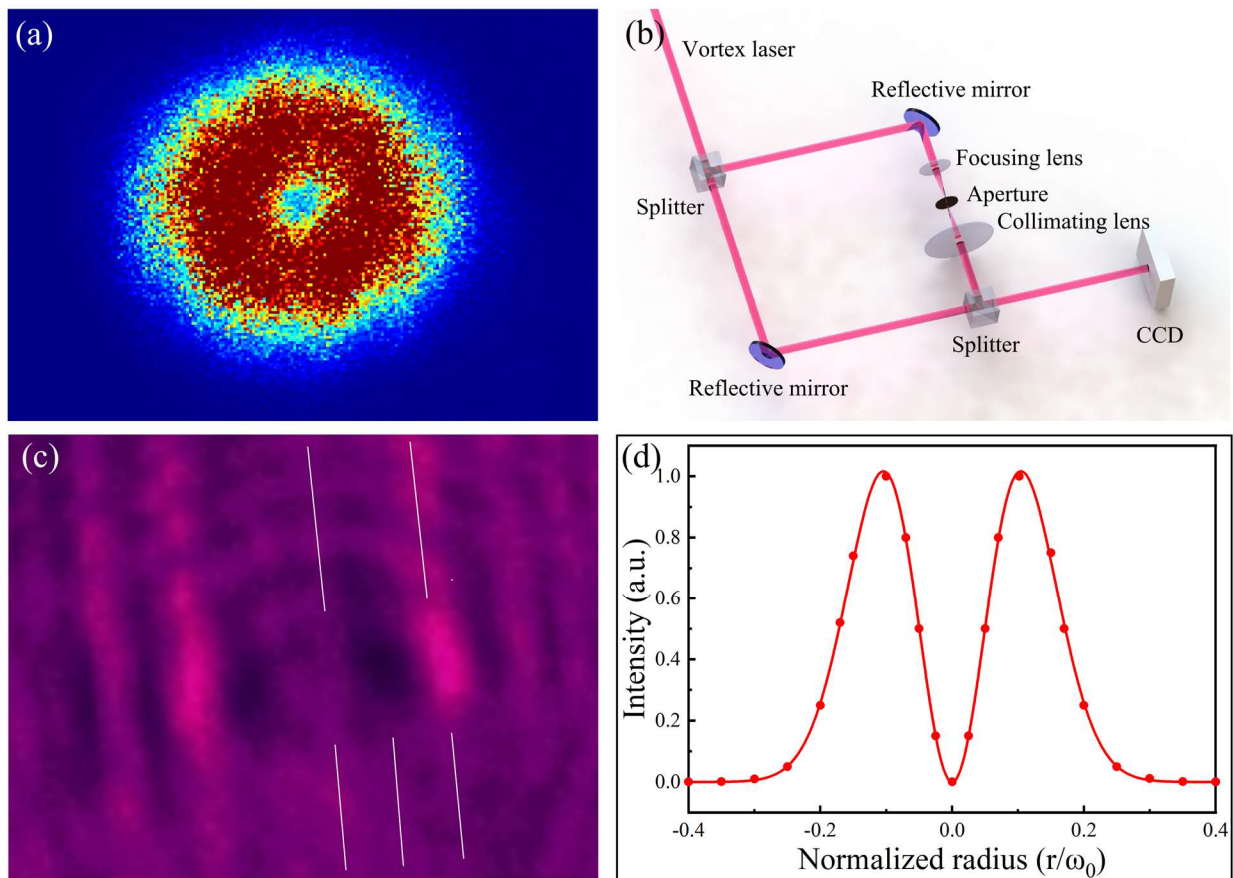


Figure 8. (a) The typical intensity profile of the high-energy vortex pulse laser; (b) The Mach-Zehnder interferometer for characterizing the topological charge of the optical vortex; (c) Beam

profiles interference patterns for vortex laser; (d) Experimentally measured transverse intensity profile and its theoretical fit.

As illustrated in Fig. 8(a), the typical intensity profile of the high-energy vortex pulse laser displays a distinctive annular light intensity pattern. To characterize the phase distribution and orbital angular momentum (OAM) carried by the output vortex laser, a custom-built Mach-Zehnder interferometer device was employed. The output intensity distribution was collected and analyzed using a CCD, as depicted in Fig. 8(b). Figure 8(c) shows the interference pattern of the vortex laser. The typical fork-shape stripe indicates that the vortex laser has a negative helical direction with a topological charge of -1. To verify the purity of the vortex mode laser, the transverse intensity profile of the vortex mode along the x-axis was measured, as shown in Fig. 8(d). The experimentally measured intensity curve is theoretically fitted by using a first-order vortex function $\frac{I}{I_0} = A \frac{2r^2}{\omega_0^2} \exp\left(-\frac{r^2}{\omega_0^2}\right)$, where $\frac{I}{I_0}$ is the normalized intensity, A is a constant, and ω_0 is the beam waist. The transverse intensity profile closely matches the theoretical fit based on the first-order vortex function, indicating excellent mode purity.

5. Conclusion

This paper has presented the first successful generation of high-energy pulsed HG and vortex lasers, using the mechanical etching defect method in conjunction with RSA HfTe₂. At an absorbed pump power of 8.15 W, the single pulse energy of the HG₁₀ laser reached 5.85 mJ with an average output power of 1.52 W. The single pulse energy of the vortex laser was 7.4 mJ, with an average output power of 1.48 W and a low repetition rate of 196 Hz. To the best of our knowledge, this is the highest single pulse energy obtained by the intra-cavity generation method. In addition, our work analyzes and verifies the advantages of the reverse saturable absorption effect in the generation of

high-energy pulses. Using an etalon, vortex pulse lasers with a tunable wavelength range of 747-787 nm were realized, thereby expanding the potential applications of high-energy HG and vortex lasers.

Acknowledgement

The authors thank the staff at the beamline BL06B at Shanghai Synchrotron Radiation Facility (SSRF) for the experimental assistance.

This work was supported by the National Natural Science Foundation of China (Grant Nos. 12204499, 12174212), and partially supported by the Joint Key Projects of National Natural Science Foundation of China (Grant No. U2032206).

References

1. S. Restuccia, D. Giovannini, G. Gibson, and M. Padgett, “Comparing the information capacity of Laguerre–Gaussian and Hermite–Gaussian modal sets in a finite-aperture system”, *Optics Express* 24, 27127-27136 (2016). DOI: <https://doi.org/10.1364/OE.24.027127>
2. K. Pang, H. Song, Z. Zhao, R. Zhang, H. Song, G. Xie, L. Li, C. Liu, J. Du, A. F. Molisch, M. Tur, and A. E. Willner, “400-Gbit/s QPSK free-space optical communication link based on four-fold multiplexing of Hermite–Gaussian or Laguerre–Gaussian modes by varying both modal indices”, *Optics Letters* 43, 3889-3892 (2018). DOI: <https://doi.org/10.1364/OL.43.003889>
3. Y. Turek, H. Kobayashi, T. Akutsu, C. P. Sun, and Y. Shikano, “Post-selected von Neumann measurement with Hermite–Gaussian and Laguerre–Gaussian pointer states”, *New J. Phys.* 17, 083029 (2015). DOI: <https://doi.org/10.1088/1367-2630/17/8/083029>
4. S. Al-Awfi, S. Bougouffa, M. Babiker, “Optical manipulation at planar dielectric surfaces using evanescent Hermite–Gaussian light”, *Optics Communications* 283, 1022-1025 (2010). DOI: <https://doi.org/10.1016/j.optcom.2009.10.119>
5. H. Liu, L. Yan, H. Chen, X. Liu, H. Liu, S. H. Chew, A. Gliserin, Q. Wang, and J. Zhang, “High-order femtosecond vortices up to the 30th order generated from a powerful mode-

- locked Hermite-Gaussian laser”, *Light Sci Appl* 12, 207 (2023). DOI: <https://doi.org/10.1038/s41377-023-01241-z>
6. G. Liang, and Q. Wang, “Controllable conversion between Hermite Gaussian and Laguerre Gaussian modes due to cross phase”, *Optics Express* 27, 10684-10691 (2019). DOI: <https://doi.org/10.1364/OE.27.010684>
 7. H. C. Liang, Y. J. Huang, Y. C. Lin, T. H. Lu, Y. F. Chen, and K. F. Huang, “Picosecond optical vortex converted from multigigahertz self-mode-locked high-order Hermite–Gaussian Nd:GdVO₄ lasers”, *Optics Letters* 34, 3842-3844 (2009). DOI: <https://doi.org/10.1364/OL.34.003842>
 8. J. Hamazaki, R. Morita, K. Chujo, Y. Kobayashi, S. Tanda, and T. Omatsu, “Optical-vortex laser ablation”, *Optics Express* 18, 2144-2151 (2010). DOI: <https://doi.org/10.1364/OE.18.002144>
 9. C. Hnatovsky, V. G. Shvedov, W. Krolikowski, and A. V. Rode, “Materials processing with a tightly focused femtosecond laser vortex pulse”, *Optics Letters* 35, 3417-3419 (2010). DOI: <https://doi.org/10.1364/OL.35.003417>
 10. O. J. Allegre, Y. Jin, W. Perrie, J. Ouyang, E. Fearon, S. P. Edwardson, and G. Dearden, “Complete wavefront and polarization control for ultrashort-pulse laser microprocessing”, *Optics Express* 21, 21198-21207 (2013). DOI: <https://doi.org/10.1364/OE.21.021198>
 11. D. Liu, Z. Kuang, W. Perrie, P. J. Scully, A. Baum, S. P. Edwardson, E. Fearon, G. Dearden, and K. G. Watkins “High-speed uniform parallel 3D refractive index micro-structuring of poly(methyl methacrylate) for volume phase gratings”, *Appl. Phys. B* 101, 817 – 823 (2010). DOI: <https://doi.org/10.1007/s00340-010-4205-5>
 12. K. Miyamoto, S. Miyagi, M. Yamada, K. Furuki, N. Aoki, M. Okida, and T. Omatsu, “Optical vortex pumped mid-infrared optical parametric oscillator”, *Optics Express* 19, 12220-12226 (2011). DOI: <https://doi.org/10.1364/OE.19.012220>
 13. L. L. N. Thi, K. F. Tsai and S. C. Chu, “Generating Optical Vortex Array Laser Beams of Superimposing Hermite–Gaussian Beams with a Dual–Phase Modulation Digital Laser System”, *Photonics* 11, 563 (2024). DOI: <https://doi.org/10.3390/photonics11060563>
 14. V. Peet, “Biaxial crystal as a versatile mode converter”, *Journal of Optics* 12, 095706 (2010). DOI: <https://doi.org/10.1088/2040-8978/12/9/095706>

15. X. Zhu, J. Yang, Y. Chen, H. He, J. Dong, “High-order Hermite-Gaussian modes and optical vortices generated in an efficient Yb:YAG microchip laser by manipulating gain distribution”, *Optics & Laser Technology* 180, 111584 (2025). DOI: <https://doi.org/10.1016/j.optlastec.2024.111584>
16. L. Hai, Z. Zhang, S. Liu, L. Li, Z. Zhou, Q. Wang, Y. Gao, C. Gao, Y. Shen, S. Fu, “Intra-Cavity Laser Manipulation of High-Dimensional Non-Separable States”, *Laser & Photonics Reviews* 18, 2300593 (2024). DOI: <https://doi.org/10.1002/lpor.202300593>
17. T. Bell, M. Kgomo, and S. Ngcobo, “Digital laser for on-demand intracavity selective excitation of second harmonic higher-order modes”, *Optics Express* 28, 16907-16923 (2020). DOI: <https://doi.org/10.1364/OE.385569>
18. Q. Yang, Z. Yang, D. Cai, X. Ren, C. Li, Y. Zu, S. Z. U. Din, J. Leng, J. Liu, and J. He, “Direct generation of continuous-wave and passively Q-switched visible vortex beams from a doughnut-shaped diode-pumped Pr:YLF laser”, *Optics Express* 30, 23909-23917 (2022). DOI: <https://doi.org/10.1364/OE.457732>
19. A. Ito, Y. Kozawa, and S. Sato, “Generation of hollow scalar and vector beams using a spot-defect mirror”, *Journal of the Optical Society of America A* 27, 2072-2077 (2010). <https://doi.org/10.1364/JOSAA.27.002072>
20. L. Tao, N. Brown, and P. Fulda, “Beam displacement tolerances on a segmented mirror for higher-order Hermite–Gauss modes”, *Journal of Optics* 26, 015603 (2024). DOI: <https://doi.org/10.1088/2040-8986/ad1120>
21. E. Cai, S. Zhang, M. Jiang, Q. Liu, F. Lou, H. Lv, and T. Li, “638-nm laser-diode pumped Alexandrite femtosecond laser passively mode-locked by single-walled carbon nanotubes”, *Optics Express* 32, 25463-25471 (2024). DOI: <https://doi.org/10.1364/OE.529959>
22. J. C. Walling, H. P. Jenssen, R. C. Morris, E. W. O’Dell, and O. G. Peterson, “Tunable-laser performance in $\text{BeAl}_2\text{O}_4:\text{Cr}^{3+}$ ”, *Optics Letters* 4, 182-183 (1979). DOI: <https://doi.org/10.1364/OL.4.000182>
23. A. Teppitaksak, A. Minassian, G. M. Thomas, and M. J. Damzen, “High efficiency >26 W diode end-pumped Alexandrite laser”, *Optics Express* 22, 16386-16392 (2014). DOI: <https://doi.org/10.1364/OE.22.016386>
24. M. Liang, A. Minassian, and M. J. Damzen, “High-energy acousto-optic Q-switched Alexandrite laser with wavelength tunable fundamental and UV second harmonic

- generation”, *Optics Express* 31, 42428-42438 (2023). DOI: <https://doi.org/10.1364/OE.505385>
25. A. I. Chizhikov, A. V. Mukhin, N. A. Egorov, V. V. Gurov, V. Y. Molchanov, N. F. Naumenko, K. V. Vorontsov, K. B. Yushkov, and N. G. Zakharov, “High-efficiency KYW acousto-optic Q-switch for a Ho:YAG laser”, *Optics Letters* 47, 1085-1088 (2022). DOI: <https://doi.org/10.1364/OL.451200>
26. J. Gong, L. Dong, H. Chu, Z. Pan, H. Pan, Y. Li, S. Zhao, D. Li, “Passively Q-switched Nd:GdVO₄ lasers with core-shell ZIF-8@ZIF-67 saturable absorber at 1 and 1.34 μm ”, *Infrared Physics & Technology* 133, 104809 (2023). DOI: <https://doi.org/10.1016/j.infrared.2023.104809>
27. E. Cai, J. Xu, S. Zhang and Z. Wu, “Tin disulfide as saturable absorber for the 1.3 μm nanosecond laser”, *Laser Phys. Lett.* 19, 065802 (2022). DOI: <https://doi.org/10.1088/1612-202X/ac6c00>
28. Y. Liang, W. Qiao, T. Feng, B. Zhang, Y. Zhao, Y. Song, T. Li, and C. Kränkel, “Investigation on the optical nonlinearity of the layered magnesium-mediated metal organic framework (Mg-MOF-74)”, *Optics Express* 29, 23786-23798 (2021). DOI: <https://doi.org/10.1364/OE.432234>
29. M. Zhang, H. He, and J. Dong, “Decentered Gaussian Beam Pumped Highly Efficient Passively Q-Switched Microchip Laser for Controllable High-Order Transverse Modes”, *IEEE Photonics Journal* 9, 1-14 (2017). DOI: <https://doi.org/10.1109/JPHOT.2017.2666552>
30. Y. Zhao, Z. Wang, H. Yu, S. Zhuang, H. Zhang, X. Xu, Jun Xu, X. Xu, J. Wang, “Direct generation of optical vortex pulses”, *Appl. Phys. Lett.* 101, 031113 (2012). DOI: <https://doi.org/10.1063/1.4737943>
31. Y. Chen, C. Chang, C. Lee, C. Sung, J. Tung, K. Su, H. Liang, W. Chen, and G. Zhang, “High-peak-power large-angular-momentum beams generated from passively Q-switched geometric modes with astigmatic transformation”, *Photonics Research* 5, 561-566 (2017). DOI: <https://doi.org/10.1364/PRJ.5.000561>
32. Y. Chen, M. Ding, J. Wang, L. Wang, Q. Liu, Y. Zhao, Y. Liu, D. Shen, Z. Wang, X. Xu, and V. Petrov, “High-energy 2 μm pulsed vortex beam excitation from a Q-switched

- Tm:LuYAG laser”, *Optics Letters* 45, 722-725 (2020). DOI: <https://doi.org/10.1364/OL.384201>
33. Q. Tian, B. Xu, N. Li, Z. Luo, H. Xu, and Z. Cai, “Direct generation of orthogonally polarized dual-wavelength continuous-wave and passively Q-switched vortex beam in diode-pumped Pr:YLF lasers”, *Optics Letters* 44, 5586-5589 (2019). DOI: <https://doi.org/10.1364/OL.44.005586>
34. N. Li; B. Xu; S. Cui; X. Qiu; Z. Luo; H. Xu; Z. Cai, and L. Chen, “High-Order Vortex Generation From CW and Passively Q-Switched Pr:YLF Visible Lasers”, *IEEE Photonics Technology Letters* 17, 1457 – 1460 (2019). DOI: <https://doi.org/10.1109/LPT.2019.2931907>
35. W. Sun, Y. Liu, C. Romero, J. R. Vázquez de Aldana, F. Ren, Y. Jia, X. Sun, and F. Chen, “Q-switched vortex waveguide laser generation based on LNOI thin films with implanted Ag nanoparticles”, *Optics Express* 31, 36725-36735 (2023). DOI: <https://doi.org/10.1364/OE.503501>
36. Y. Pan, M. Zhang, and J. Dong, “Orientation and separation controllable dual-vortex passively Q-switched microchip laser”, *Journal of Optics* 21, 085202 (2019). DOI: <https://doi.org/10.1088/2040-8986/ab2967>
37. J. Liu, Y. Duan, W. Mao, X. Jin, Z. Li, and H. Zhu, “An Axicon-Based Annular Pump Acousto-Optic Q-Switched Nd:GdVO₄ Self-Raman Vortex Laser”, *Crystals* 13, 1484 (2023). DOI: <https://doi.org/10.3390/cryst13101484>
38. Q. Liu, Y. Zhao, W. Zhou, and D. Shen, “Vortex operation in Er:LuYAG crystal laser at ~1.6 μm”, *Optical Materials* 71, 31-34 (2017). DOI: <https://doi.org/10.1016/j.optmat.2016.06.034>
39. W. Zhang, L. Tong, Y. Yuan, C. Chen, Y. Cai, and L. Zhao, “Self-Q-switched Tm:YAP vortex laser by thermal-lensing effect”, *Infrared Physics & Technology* 123, 104197 (2022). DOI: <https://doi.org/10.1016/j.infrared.2022.104197>
40. L. Tong, C. Chen, Y. Cai, and L. Zhao, “Pulsed Optical Vortex Array Generation in a Self-Q-Switched Tm:YALO₃ Laser”, *Materials* 17, 1144 (2024). DOI: <https://doi.org/10.3390/ma17051144>

41. K. Huang, C. Su, M. Lin, Y. Chiu, and Y. Huang, “Efficient 750-nm LED-pumped Nd:YAG laser”, *Optics Express* 24, 12043-12054 (2016). DOI: <https://doi.org/10.1364/OE.24.012043>
42. S. Micalizio, F. Levi, C. E. Calosso, M. Gozzelino, and A. Godone, “A pulsed-Laser Rb atomic frequency standard for GNSS applications”, *GPS Solut* 25, 94 (2021). DOI: <https://doi.org/10.1007/s10291-021-01136-9>
43. C. Wang, C. Lee, Y. Kim, and Y. Kim, “Generation of hyper-entangled photons in a hot atomic vapor”, *Optics Letters* 45, 1802-1805 (2020). DOI: <https://doi.org/10.1364/OL.384567>
44. A. J. McCulloch, D. V. Sheludko, M. Junker, and R. E. Scholten, “High-coherence picosecond electron bunches from cold atoms”, *Nature Communications* 4, 1692 (2013). DOI: <https://doi.org/10.1038/ncomms2747>
45. M. Kim, R. Notermans, C. Overstreet, J. Curti, P. Asenbaum, and M. A. Kasevich, “40 W, 780 nm laser system with compensated dual beam splitters for atom interferometry”, *Optics Letters* 45, 6555-6558 (2020). DOI: <https://doi.org/10.1364/OL.404430>
46. M. Hübner, M. Wilkens, B. Eppich, A. Maaßdorf, D. Martin, A. Ginolas, P. S. Basler, and P. Crump, “A 1.4 kW 780 nm pulsed diode laser, high duty cycle, passively side-cooled pump module”, *Optics Express* 29, 9749-9757 (2021). DOI: <https://doi.org/10.1364/OE.416527>
47. C. Ke, C. Chen, M. Yang, H. Chen, Y. Ke, and L. Li, “Inhibition of infantile hemangioma growth and promotion of apoptosis via VEGF/PI3K/Akt axis by 755-nm long-pulse Alexandrite laser”, *Biomedical Journal* 47, 100675 (2024). DOI: <https://doi.org/10.1016/j.bj.2023.100675>
48. M. Chi, A. Müller, A. K. Hansen, O. B. Jensen, P. M. Petersen, and B. Sump, “Micro-integrated high-power narrow-linewidth external-cavity tapered diode laser at 762 nm for daylight imaging”, *Optics Communications* 514, 128120 (2022). DOI: <https://doi.org/10.1016/j.optcom.2022.128120>
49. Q. Li, W. Perrie, R. Potter, O. Allegre, Z. Li, Y. Tang, G. Zhu, D. Liu, P. Chalker, and J. Ho, “Femtosecond laser micro-structuring of amorphous polyether(ether)ketone at 775 nm and 387 nm”, *J. Phys. D: Appl. Phys.* 53, 365301 (2020). DOI: <https://doi.org/10.1088/1361-6463/ab8ed8>

50. M. Maiwald, B. Eppich, A. Ginolas, B. Sumpf, G. Erbert, and G. Tränkle, “Compact Handheld Probe for Shifted Excitation Raman Difference Spectroscopy with Implemented Dual-Wavelength Diode Laser at 785 Nanometers”, *Applied Spectroscopy*, 69, 1144-1151 (2015). DOI: <https://doi.org/10.1366/15-07858>